Path suppression of strongly collapsing bubbles at finite and low Reynolds numbers

Ludmila M. Rechiman,* Damián Dellavale, and Fabián J. Bonetto
Instituto Balseiro/UNCu/CNEA/CONICET, Av. Bustillo Km. 9.5, S.C. de Bariloche, RN, Argentina
(Received 18 December 2012; revised manuscript received 26 February 2013; published 6 June 2013)

We study, numerically and experimentally, three different methods to suppress the trajectories of strongly collapsing and sonoluminescent bubbles in a highly viscous sulfuric acid solution. A new numerical scheme based on the *window method* is proposed to account for the history force acting on a spherical bubble with variable radius. We could quantify the history force, which is not negligible in comparison with the primary Bjerknes force in this type of problem, and results are in agreement with the classical primary Bjerknes force trapping threshold analysis. Moreover, the present numerical implementation reproduces the spatial behavior associated with the positional and path instability of sonoluminescent argon bubbles in strongly gassed and highly degassed sulfuric acid solutions. Finally, the model allows us to demonstrate that spatially stationary bubbles driven by biharmonic excitation could be obtained with a different mode from the one used in previous reported experiments.

DOI: 10.1103/PhysRevE.87.063004 PACS number(s): 78.60.Mq, 43.25.Yw, 47.20.Gv

I. INTRODUCTION

Bubbles can respond to a driving pressure field in a nonlinear way if the pressure applied on the bubble is larger than the Blake threshold achieving high compression rates [1]. Single Bubble Sonoluminescence (SBSL) is an example of energy focusing phenomena that use this fact and a more efficient compression could be achieved for spatially fixed bubbles.

As the main goal is to achieve higher temperatures of the inside bubble contents, liquids with low vapor pressure, such as sulfuric acid solutions [2–7], phosphoric acid solutions [8], and ethylene glycol [9], have been used by many researchers. The presence of vapor during main collapse does not favor the goal to achieve higher energy concentrations and higher temperatures because water dissociation processes absorb part of the mechanical energy available [10]. On the other hand, these liquids have the property that they are several times more viscous than water. This property has a stabilizing effect on the development of shape instabilities when the amplitude of the forcing pressure field rises [5,11].

Experiments made with argon bubbles in these liquids revealed that the bubble not only oscillates in a radial way but also can translate through the viscous liquid describing quasiperiodic trajectories (moving-SBSL). The hydrodynamic force responsible for this spatial-instability is the history force [9]. Typically, the experimental characterization of the radial dynamics of the bubble requires the bubble to be in a spatially fixed position [6], because by adjusting the measurements of the evolution of the bubble radius as function of time with a suitable numerical model, the amplitude of the driving pressure on the bubble wall, the amount of noncondensible gas, and the reached temperature of the gas contents are determined.

In this paper, we shed light on the different mechanisms to suppress the trajectories of strongly collapsing bubbles at finite and low Reynolds numbers in the parameter range in which the bubble is sonoluminescent. We study, experimentally and numerically, three mechanisms to spatially stabilize bubbles: (1) By driving the bubble with amplitudes of the pressure field in the fundamental mode low enough, (2) by driving bubbles in a liquid with a very low concentration of noncondensible gas dissolved in the liquid, and (3) by driving the bubble with a multifrequency excitation.

The paper is organized as follows: in Sec. II we detail the main features of the implemented model; in Sec. III, Sec. IV, and Sec. V we describe the different methods to obtain spatially fixed bubbles in the nonlinear regime; and, finally, in Sec. VI we summarize our conclusions.

II. NUMERICAL MODEL

We solved the radial dynamics of a bubble described by the Rayleigh-Plesset-Keller equation [12] coupled with the translational dynamics following the model of the viscous forces detailed in Ref. [13]. The latter is obtained by applying Newton's second law to a nonspinning bubble with variable radius taking into account the following forces: primary Bjerknes force ($\vec{F}_{\text{Bjerknes}}$) [1], added mass force ($\vec{F}_{\text{am}}$) [14], steady-drag force ($\vec{F}_{\text{Drag}}$) [15], buoyant force ($\vec{F}_{\text{boy}}$) [14], and history force ($\vec{F}_{\text{history}}$) [13]. The radial dynamics of the bubble is fully dependent on the model used to compute the thermodynamical evolution of the noncondensible gas inside the bubble. We used a model that represent the isothermal evolution of the gas during the rarefaction phase of the acoustic cycle (expansion of the bubble) and the adiabatic evolution in the final stage of main collapse by using a variable polytropic coefficient given by Ref. [16]. To use this closing equation we assume a Van der Waals gas and uniform profiles for the pressure and temperature inside the bubble. Then the dynamical system that coupled the radial and translational dynamics of a periodically driven strongly collapsing bubble

*rechimal@ib.cnea.gov.ar

located in a viscous liquid is

$$\begin{cases} \left[1-\frac{\dot{R}(t)}{c_l}\right]R(t)\ddot{R}(t)+\frac{3}{2}\dot{R}^2(t)\left[1-\frac{\dot{R}(t)}{3c_l}\right]=\frac{1}{\rho_l}\left[1+\frac{\dot{R}(t)}{c_l}\right][p_g(R(t))-p(r,t)]+\frac{R(t)\dot{p}_g(R(t))}{\rho_l c_l}-\frac{4\nu_l\dot{R}(t)}{R(t)}-\frac{2\sigma}{\rho_l R(t)} \\ \dot{T}_b=-[\gamma(R,\dot{R},T_b)-1]\frac{3R^2(t)\dot{R}(t)}{R^3(t)-h^3}T_b(t)-\chi_g\frac{T_b(t)-T_0}{R^2(t)} \\ \vec{F}_b=-\frac{4}{3}\pi R^3(t)\vec{\nabla}p(r,t)-\frac{2}{3}\pi\rho_l\frac{d(R^3(t)\vec{U}(r,t))}{dt}-6\pi\rho_l\nu_l R(t)\vec{U}(r,t)-\frac{4}{3}\pi\rho_l R^3(t)\vec{g} \quad \text{if} \quad \mathrm{Re}_t \text{ or } \mathrm{Re}_r \gg 1 \\ \vec{F}_b=-\frac{4}{3}\pi R^3(t)\vec{\nabla}p(r,t)-\frac{2}{3}\pi\rho_l\frac{d(R^3(t)\vec{U}(r,t))}{dt}-6\pi\rho_l\nu_l R(t)\vec{U}(r,t)-\frac{4}{3}\pi\rho_l R^3(t)\vec{g}- \\ \quad -8\pi\rho_l\nu_l\int_0^t \exp\left[9\nu\int_\tau^t\frac{1}{R^2(s)}ds\right]\mathrm{erfc}\left[\sqrt{9\nu\int_\tau^t\frac{1}{R^2(s)}ds}\right]\frac{d}{d\tau}(R(\tau)\vec{U}(r,\tau))d\tau \quad \text{if} \quad \mathrm{Re}_t \text{ and } \mathrm{Re}_r \ll 1 \end{cases} \tag{1}$$

In the system represented by Eqs. (1), t is the time, $R(t)$ is the radius of the bubble, $\dot{R}(t)$ is the radial velocity of the bubble interface, $\ddot{R}(t)$ is the radial acceleration of the bubble interface, ρ_l is the liquid density, c_l is the speed of sound in the liquid, σ is the surface tension, ν_l is the kinematic viscosity of the liquid, $p_g(R(t))$ is the pressure of the gas contents inside the bubble, and $p(r,t)$ denotes the driving pressure field. T_b is the temperature of the gas contents inside the bubble, $\gamma(R,\dot{R},T_b)$ is the variable polytropic coefficient, $\chi_g(t)$ denotes the thermal diffusivity of the gas, T_0 is the ambient temperature, and h is the Van der Waals hard core radius of the gas. r is the radial coordinate; $r_b(t)=\sqrt{x(t)^2+y(t)^2+z(t)^2}$ is the distance from the center of the bubble to the origin of coordinates, which is located in the middle of a spherical resonator; $x(t)$, $y(t)$, and $z(t)$ indicate the location of the center of the bubble in Cartesian coordinates; $\vec{U}(r,t)=\vec{V}_b-\vec{u}_l(r,t)$ is the relative velocity between the bubble translational velocity and the liquid velocity, and $\vec{g}$ is the gravity acceleration.

These equations form a nonautonomous dynamical system which it is solved with the smallest time scale, that is the one ruled by the radial dynamics in response to the external driving pressure. In particular, the system of Eqs. (1) was solved by double-stepping adaptive step-size Runge-Kutta algorithm [17] to obtain the solutions of $(R(t),\dot{R}(t),T_b(t),x(t),\dot{x}(t),y(t),\dot{y}(t),z(t),\dot{z}(t))$. It is important to point out that in the present work we do not neglect the inertia of the bubble, then the total force acting on the bubble is $\vec{F}_b=m_b\vec{a}_b\neq 0$, where m_b is the mass of the bubble and $\vec{a}_b$ is the translational acceleration of the bubble. For the steady-drag force of the present model we take into consideration a dirty bubble case [15], due to the fact that bubbles of less than 100 μm are more likely to suffer surfactant deposition on its surface [1,15]. Regarding the history force, we follow the model described in Ref. [13] and we applied a suitable approximation of the kernel of the history force integral [18]:

$$\vec{F}_{\text{history}}\simeq 8\pi\rho_l\nu_l\int_0^t\frac{a}{(a-1)\sqrt{\pi 9\nu_l\int_\tau^t\frac{1}{R^2(s)}ds}+\sqrt{\pi 9\nu_l\int_\tau^t\frac{1}{R^2(s)}ds+a^2}}\frac{d}{d\tau}(R(\tau)\vec{U}(r,\tau))d\tau \tag{2}$$

In Eq. (2), t denotes the time from the beginning of the evolution and a is a constant equal to $a=2.9110$. This value for a is selected as the one that minimizes the relative error, which is lower than $<0.3\%$ for a wide range of $H=9\nu_l\int_\tau^t\frac{1}{R^2(s)}ds$ arguments [19]. Further details can be seen in Appendix A. By using this approximation we avoid overflow problems in the case of large H values. Moreover, the history force is not acting during the whole radial period [19]. To condense both descriptions for the different Reynolds numbers, we implement the switches described in Ref. [9] with the same threshold values. In the present work we solve the integrodifferential equation for bubble position with an approach that differs from the one implemented by Ref. [9]. We solved Eq. (2) for each time step of the bubble evolution by applying the *window method* [20]. This method was first implemented by Dorgan and Loth [20] to solve the integral of the Basset force acting on fixed-size particles, denser than the host liquid and in ranges where the fluid dynamics around the body can be well described by a creeping flow. Later, this study was extended by Loth and Dorgan [21] to analyze bubbles and

TABLE I. Properties at 20 °C of sulfuric acid solution SO_4H_2(85%wt)-H_2O(15%wt) [23–25].

Property	Value
Density, ρ_l	1778.6 kg/m^3
Dynamic viscosity, μ_l	0.015 Pa s
Kinematic viscosity, ν_l	8.4×10^{-6}m^2/s
Speed of sound, c_l	1473.0 m/s
Vapor pressure, p_v	2.45 Pa
Surface tension, σ	0.074 N/m

optimized in accuracy and time by van Hinsberg *et al.* [22], but all these studies were developed for spherical particles with a fixed radius. Although in the present work we deal with bubbles with variable radius, the common fact in both cases is that the most time and memory consuming term in the translational equation of motion is the term related with history force. The main advantage of the window method is to reduce the calculation time and memory requirements by making the integration of Eq. (2) over a finite time interval (t_{win}).

For the truncated integration interval, the length of the backward window is defined as the time in which the term $\frac{d(RU)}{dt}$ in Eq. (2) remains nearly constant [20]. In this research, the integration over the window was made by applying the two-point closed Newton-Cotes formula. For the liquid used in the present work, a solution of 85% wt sulfuric acid and 15% wt water (SA85), the window length is approximately half the radial period [19]. A wider explanation for the determination of the window length is displayed in Appendix B. The properties of SA85 are summarized in Table I. The main advantage of the present implementation in comparison with previous numerical schemes is that it allows the calculation of the history force value at each time instant.

The external pressure field with an explicit dependence with time and considering a spherical geometry with bi-harmonic excitation is $p(r,t) = p_\infty - \frac{\sin(k_0 r)}{k_0 r} p_a^0 \sin(2\pi f_0 t) - \frac{\sin(k_n r)}{k_n r} p_a^n \sin(2\pi n f_0 t + \phi)$. Here p_∞ is the static pressure of

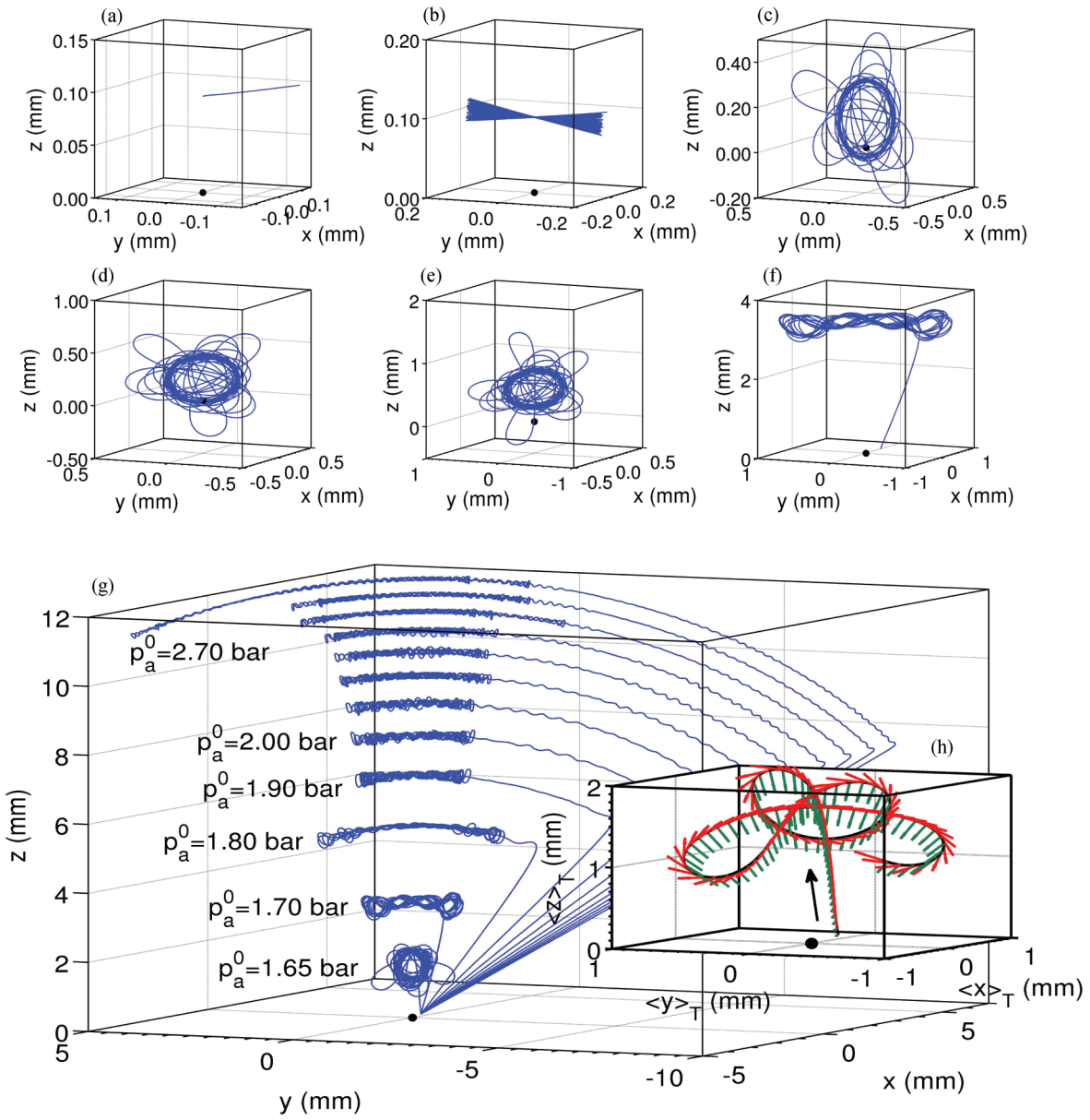

FIG. 1. (Color online) (a)–(g) Trajectories of an argon bubble with $R_0 = 9.0\ \mu$m in SA85 driving at $f_0 = 30$ kHz under different pressure amplitudes at the resonator center (p_a^0). (a) $p_a^0 = 1.30$ bar. (b) $p_a^0 = 1.32$ bar. (c) $p_a^0 = 1.40$ bar. (d) $p_a^0 = 1.50$ bar. (e) $p_a^0 = 1.60$ bar. (f) $p_a^0 = 1.70$ bar. The black dot indicates the origin of coordinates. (g) $p_a^0 = 1.65$ bar, $p_a^0 = 1.70$ bar, $p_a^0 = 1.80$ bar, $p_a^0 = 1.90$ bar, $p_a^0 = 2.00$ bar, $p_a^0 = 2.10$ bar, $p_a^0 = 2.20$ bar, $p_a^0 = 2.30$ bar, $p_a^0 = 2.40$ bar, $p_a^0 = 2.50$ bar, $p_a^0 = 2.60$ bar, and $p_a^0 = 2.70$ bar. (h) The inset shows for the case with $p_a^0 = 1.65$ bar, the direction of the F_{history} (red) and F_{Bjerknes} (green) for the first 1500 radial cycles.

the system, the subscript "0" denotes the fundamental mode, while the "n" letter denotes the harmonic. k_0 and k_n are the wave numbers, r is the radial distance from the center of the resonator, f_0 and f_n are the driving frequencies, and ϕ is the relative phase between the signals. The radial period of the fundamental frequency is denoted by $T = \frac{1}{f_0}$. p_a^0 and p_a^n are the amplitudes of each component of the pressure field at the resonator center, which are controllable parameters. On the other hand, we denote the amplitudes of the pressure of each frequency component applied on the bubble at position r_b as $p_a^{b\mathrm{LF}} = \frac{\sin(k_0 r_b)}{k_0 r_b} p_a^0$ and $p_a^{b\mathrm{HF}} = \frac{\sin(k_n r_b)}{k_n r_b} p_a^n$, which are nearly the same as the amplitudes of the pressure at resonator center if the bubble mean position is not far from the resonator center. It should be pointed out that we considered that the spatial dependence of the pressure field in the fundamental mode and in the harmonic frequency are strictly radial. With the proposed pressure field, the liquid velocity can be analytically calculated by linearizing the Navier-Stokes equation and neglecting viscous stress and volume forces [9].

III. PATH SUPPRESSION BY DRIVING THE BUBBLE WITH LOW AMPLITUDES OF THE PRESSURE FIELD IN THE FUNDAMENTAL MODE

In Fig. 1 the trajectories of an argon bubble in SA85 are shown under different (p_a^0). In particular, Figs. 1(a)–1(f) shows the transition from a nonmoving state to a moving state when p_a^0 rises. The initial position of the bubble for these simulations was $x_i = 0.10$ mm, $y_i = -0.15$ mm, and $z_i = 0.10$ mm and moves towards an upper point from the center. Figure 1(g) shows how the mean levitation position shifts away from the center due to the positional instability when p_a^0 increases and in the vertical direction due to the buoyant force. Figure 1(h) shows, for the $p_a^0 = 1.65$ bar case, the history and primary Bjerknes force averaged in a radial period. The former is responsible for the path instability [9], while the latter is responsible for the trapping of the bubble at the pressure antinode for this particular size of bubbles, which are smaller than resonant Minnaert radius for the range of parameters treated in the present work [26]. It can be seen that the history force direction coincides with the direction of movement of the bubble, while the primary Bjerknes force is the only force considered in this model that is not tangent to the bubble trajectory and acts like a centripetal force. In Fig. 2, the onset of the path instability at $p_a^0 = 1.32$ bar, as well as the onset of positional instability at $p_a^0 = 1.60$ bar, can be seen. We refer to "positional instability" to the shifting from the center of the resonator of the mean levitation location of the bubble, while "path instability is the state when the bubble describes pseudo-orbits. Further numerical simulations of bubbles with different ambient radius (R_0) reveal that the onset of moving bubbles occurs for bubbles with $R_0 > 8$ μm and the $p^0_{a_{\mathrm{onsetPathI}}} \simeq p^b_{a_{\mathrm{onsetPathI}}}$ decreases monotonically with the increment of the ambient radius. Moreover, no path instability was obtained for bubbles with $R_0 < 8$ μm for a wide range of pressures at the resonator center 1.20 bar $< p_a^0 <$ 2.70 bar. From Fig. 3 it can be seen that the diffusively stability condition given by the ratio ($\frac{c_\infty}{c_0}$) [27] does not remain in a constant value when p_a^0 rises if only the ambient radius is held fixed.

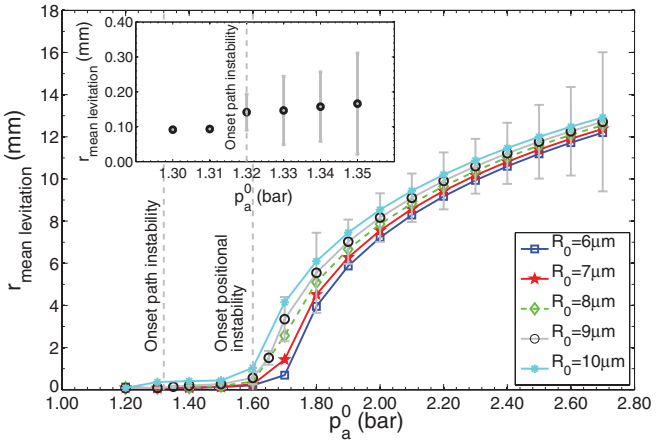

FIG. 2. (Color online) Mean levitation distance as function of p_a^0 using the ambient radius R_0 as a parameter for argon bubbles in SA85 solution driven at $f_0 = 30$ kHz. The gray bars indicate the approximate maximum amplitude of the pseudo-orbits for the particular case of $R_0 = 9$ μm. For driving pressures below $p_a^0 < 1.31$ bar no pseudo-orbits appeared. The onset of the path instability at $p_a^0 = 1.32$ bar as well as the onset of the positional instability at $p_a^0 = 1.60$ bar, is indicated with gray dotted line. The inset shows in detail the transition between the *non-moving bubble* and the *moving-bubble* for the particular case of $R_0 = 9$ μm.

A wider study of the hydrodynamic forces was made for bubbles with different amounts of noncondensible gas. In Fig. 4 it is shown that the primary Bjerknes force magnitude averaged in a radial cycle has a drastic and monotonic growth with the onset of positional instability, ranging between $p_a^0 = 1.60$ bar and $p_a^0 = 1.70$ bar for a $R_0 = 10$ μm and $R_0 = 6$ μm, respectively. This shows that the primary Bjerknes force increases when p_a^0 rises and it has a greater magnitude for larger bubbles. In Fig. 5, we also show that when p_a^0 rises, the history force averaged in a radial cycle reaches a nearly stationary fixed value. In particular, for an $R_0 = 9$ μm bubble is $\langle F_{\mathrm{history}} \rangle_T \sim 0.43$ μN. A similar behavior is observed for the maximum magnitude of the added mass or added mass peak ($\vec{F}_{\mathrm{am}}^{\max}$) that is spikelike at main collapse, which in the

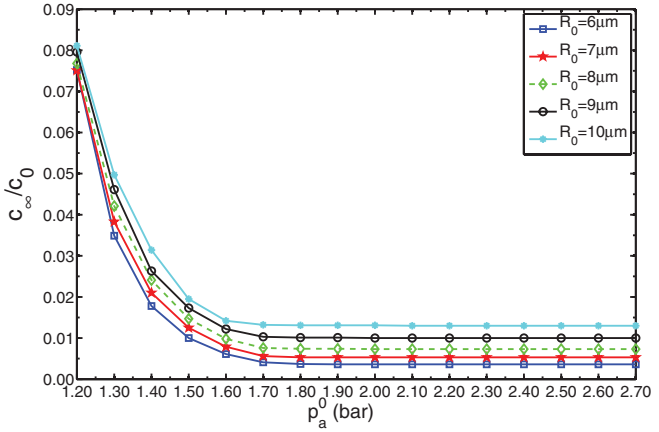

FIG. 3. (Color online) Ratio $\frac{c_\infty}{c_0}$ as a function of p_a^0 for different R_0 for argon bubbles in SA85 solution driven at $f_0 = 30$ kHz. For $p_a^0 > 1.70$ bar, a plateau is reached in all cases studied.

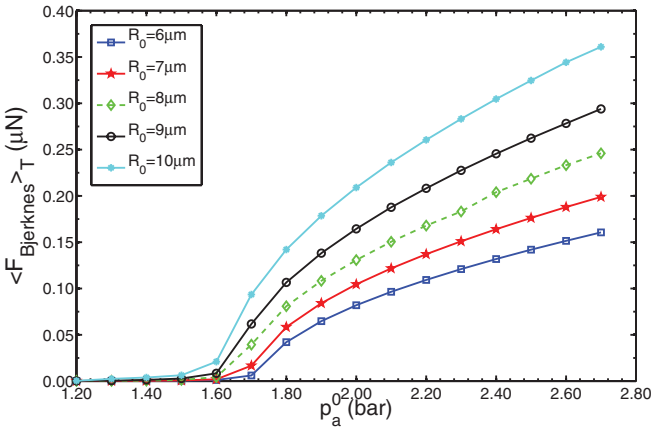

FIG. 4. (Color online) Primary Bjerknes force module averaged in each radial cycle using the ambient radius as a parameter for an argon bubble in SA85 driven at 30 kHz.

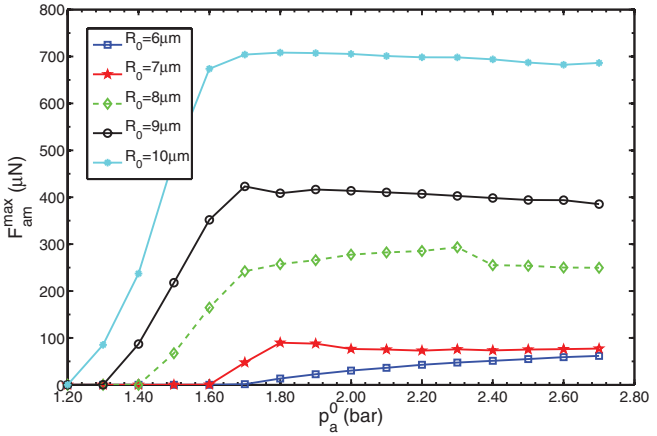

FIG. 6. (Color online) Added mass peak force module using the ambient radius as a parameter for an argon bubble in SA85 driven at 30 kHz.

case of an $R_0 = 9$ μm bubble is $|F_{\rm am}^{\rm max}| \sim 434$ μN (Fig. 6). This behavior of the added mass force is the responsible for the larger translational movements of the bubble during main collapse [19,28]. This implies that the accuracy of the translational displacement of the bubble is highly sensitive with the accuracy of the added mass force and radial velocity of the bubble interface ($\dot{R}$) calculations. In Appendix C we show an error analysis of how small discrepancies in the calculation of ($\dot{R}$) have an influence on the added mass peak force.

IV. PATH SUPPRESSION BY DRIVING THE BUBBLE IN A LIQUID WITH A VERY LOW CONCENTRATION OF DISSOLVED NONCONDENSIBLE GAS

It should be noted that in a real experiment the gas concentration diluted in the liquid remains constant, and then, to allow for comparison with experiments, the ratio between the concentration far away from the bubble and the saturation concentration ($\frac{c_\infty}{c_0}$) [27] was maintained at a fixed value. In Fig. 7, the phase space for argon bubbles in SA85 driven at 29 200 Hz is shown. The primary Bjerknes trapping threshold [11,26], the diffusive contours [27], the parametric shape instability boundary [29], and the Blake threshold [1] are also displayed. Two experiments were carried out: (case I) driving pressure ramp for an argon bubble in SA85 with a high gas concentration diluted in the liquid ($\frac{c_\infty}{c_0} = 0.017$)

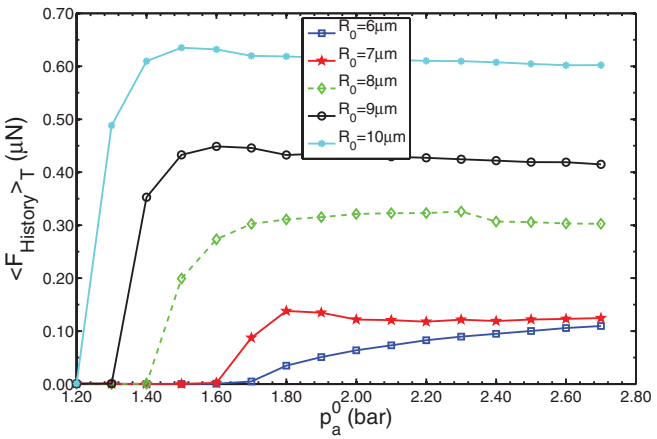

FIG. 5. (Color online) History force module averaged in each radial cycle using the ambient radius as a parameter for an argon bubble in SA85 driven at 30 kHz.

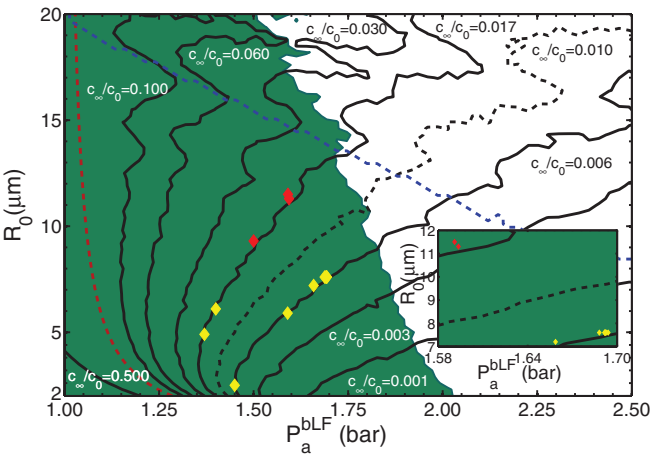

FIG. 7. (Color online) Phase diagram of an argon bubble driving at $f_0 = 29.2$ kHz in SA85. (green line) Indicates the trapping threshold due to primary Bjerknes force for bubbles that remain spatially fixed in the pressure field driven by p_a^{bLF}. In green is shown the region where the primary Bjerknes force is able to trap the bubble near the central antinode of pressure, while in white is shown the region where the bubble is repealed from the central antinode of pressure. (Solid black line) Indicates different diffusive constant contour levels ($\frac{c_\infty}{c_0}$ = cte). (Dotted black line) The contour $\frac{c_\infty}{c_0} = 0.010$ indicates the threshold between low and high gas concentration dissolved in the liquid. (dotted blue line) Indicates the parametric shape instability boundary calculated using the vorticity boundary layer approximation [29]. (Red dotted line) Indicates the Blake threshold, which marks the onset of nonlinear bubble response to the acoustic pressure. (Red dots) Indicate moving bubbles. (Yellow dots) Indicate nonmoving bubbles. (Inset) Shows the accumulative points. When p_a^0 rises, the bubble shifts away from the center and lower pressures are applied on the bubble wall up to an asymptotic value. For $\frac{c_\infty}{c_0} = 0.017$ the asymptotic value is $p_a^{bLF} = 1.59$ bar, while for $\frac{c_\infty}{c_0} = 0.006$, $p_a^{bLF} = 1.69$ bar.

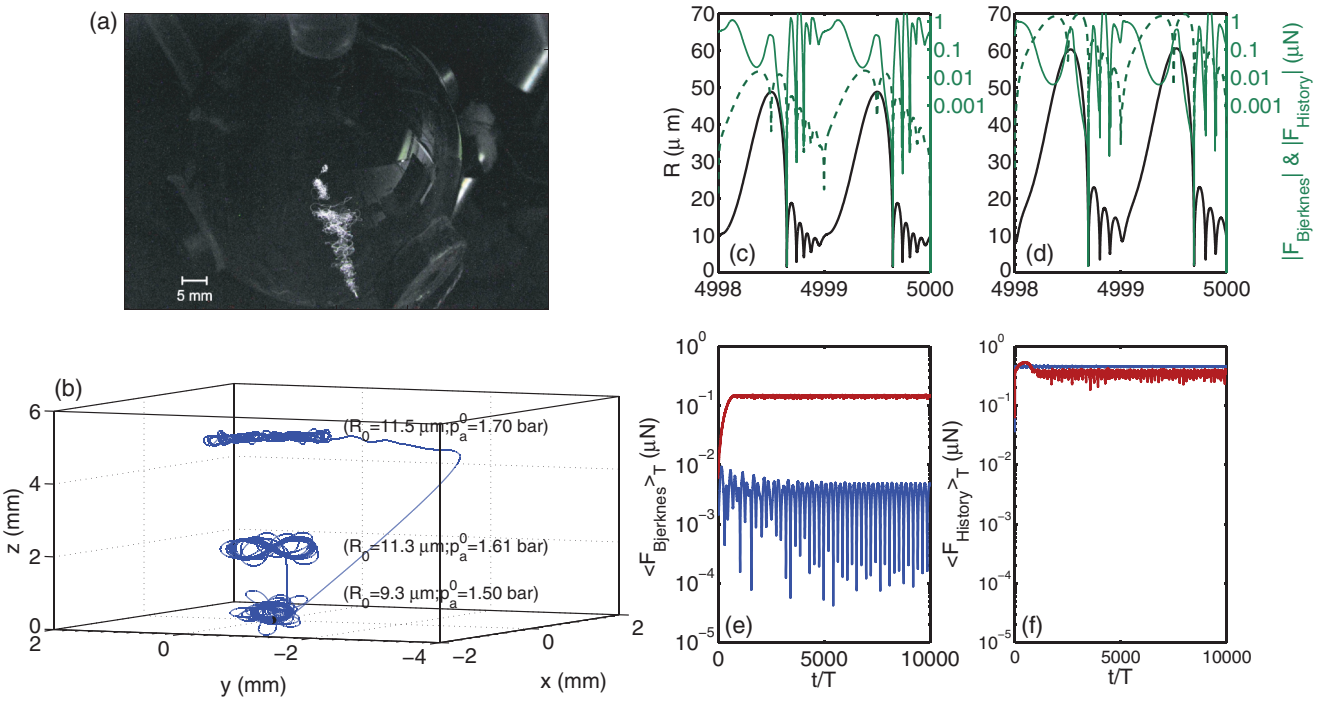

FIG. 8. (Color online) (a) SL argon bubble in SA85 driven only with a frequency equivalent to the first eigenvalue of the resonator ($f_0 = 29.2$ kHz). The experiment was made with a high gas concentration diluted in the liquid ($\frac{c_\infty}{c_0} = 0.017$). p_a^0 was gradually increased in a quasistatic manner [32]. (b) Numerical simulations keeping constant $\frac{c_\infty}{c_0}$ as in the real experiment. For the selected concentration ($\frac{c_\infty}{c_0} = 0.017$), the numerical model reproduces the "path instability" as well as the "positional instability" when p_a^0 rises. (c) (Black line) Temporal evolution of the bubble radius ($R_0 = 9.3$ μm; $p_a^0 = 1.50$ bar), positional stable and path unstable case. (Solid green line) Module of the history force acting on the bubble in the radial time scale. (Dotted green line) Module of the primary Bjerknes force. (d) (Black line) Temporal evolution of the bubble radius ($R_0 = 11.5$ μm; $p_a^0 = 1.70$ bar), positional unstable and path unstable case. (Solid green line) Module of the history force acting on the bubble in the radial time scale. (Dotted green line) Module of the primary Bjerknes force. (e) Module of the primary Bjerknes force in the time scale of spatial trajectories. The simulations were made during 10 000 radial cycles. (Blue line) Case ($R_0 = 9.3$ μm; $p_a^0 = 1.50$ bar), positional stable and path unstable case. (Red line) Case ($R_0 = 11.5$ μm; $p_a^0 = 1.70$ bar), positional unstable and path unstable case. (f) Module of the history force in the time scale of spatial trajectories. The simulations were made during 10 000 radial cycles. (Blue line) Case ($R_0 = 9.3$ μm; $p_a^0 = 1.50$ bar), positional stable and path unstable case. (Red line) Case ($R_0 = 11.5$ μm; $p_a^0 = 1.70$ bar), positional unstable and path unstable case.

and (case II) driving pressure ramp for an argon bubble in SA85 with a low gas concentration diluted in the liquid ($\frac{c_\infty}{c_0} = 0.006$). The experiments show the absence of the path instability for ($\frac{c_\infty}{c_0} < 0.010$) [7]. The dots in Fig. 7 show the cases simulated with the present model, where the trapping threshold calculated with the classical positional analysis is overestimated, and the differences may be due to the complex dynamical equilibrium between all the hydrodynamic forces considered with this model. To keep constant $\frac{c_\infty}{c_0} = cte$, an iterative process in the calculations was required. We used as seeds the pairs (p_a^b,R_0) obtained with the model without coupling the translational part for the selected concentration. In the model with the translational part included, we used $p_a^0 = p_a^b$. For small pressures at the resonator center the bubble displaces to a position near the center, the pressure at bubble wall is not diminished by the spatial influence given by the spherical Bessel function J_0, and then the $\frac{c_\infty}{c_0}$ is approximately the required one. When p_a^0 is such that the final bubble levitation position is away from the center, the pressure at bubble wall is lower than the pressure at the resonator center ($p_a^b < p_a^0$). In Fig. 7 it means that the ratio ($\frac{c_\infty}{c_0}$) rises (shifts towards left). The next step in the iterative process will remain the same p_a^0 while the ambient radius R_0 is diminished. These steps are repeated until the ratio ($\frac{c_\infty}{c_0}$) is the desired one. It can also be seen in Fig. 7, that although p_a^0 increases, the pressure applied on bubble wall p_a^b at position r_b tends to be constant, and this fact is represented as accumulation points. For high gas concentration of gas diluted in the liquid (case I), the transition between nonmoving bubbles and moving bubbles could be simulated. The last is displayed with yellow and red dots respectively in Fig. 7. Moreover, it can be seen from Fig. 8(a) and Fig. 8(b) that the numerical simulations correctly reproduce the experimental observations of the path instability and positional instability. In Figs. 8(c) and 8(d), the history force during bubble radius evolution is shown in detail. It can be seen that the action of the history force occurs while the bubble is expanding and during each maximum of the bubble rebounds. In addition, the primary Bjerknes force module and history force module, both averaged in a radial period, are more comparable when p_a^0 rises, while for lower p_a^0 the magnitude of the history force could be larger than the magnitude of the primary Bjerknes force [Fig. 8(e) and Fig. 8(f)]. For bubbles in a SA85 with low gas concentration (case II), no path instability could be experimentally observed neither simulated for a wide

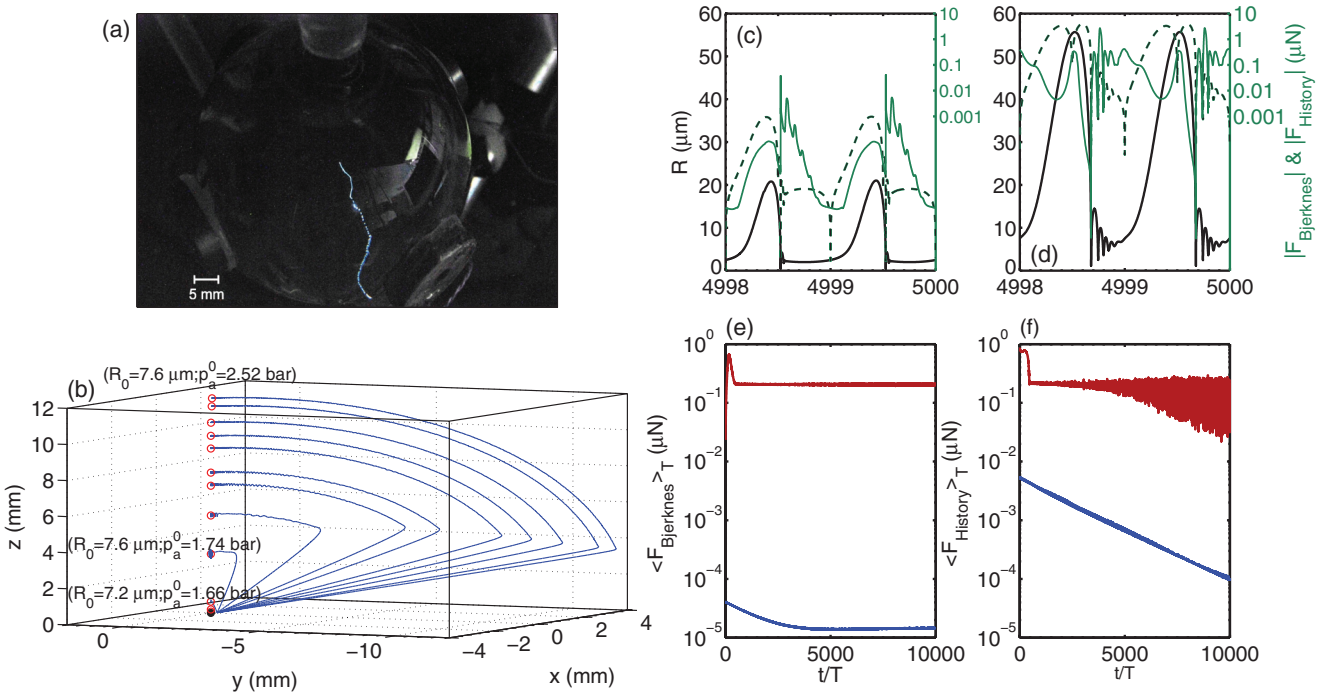

FIG. 9. (Color online) (a) SL argon bubble in SA85 driven only with a frequency equivalent to the first eigenvalue of the resonator ($f_0 = 29.2$ kHz). The experiment was made with a low gas concentration diluted in the liquid ($\frac{c_\infty}{c_0} = 0.006$). p_a^0 was gradually increased in a quasistatic manner [32]. (b) Numerical simulations keeping constant $\frac{c_\infty}{c_0}$ as in the real experiment. For the selected concentration ($\frac{c_\infty}{c_0} = 0.006$), the numerical model reproduces the mean levitation position shifting away from the center when p_a^0 rises ("positional instability"). No "path instability" could be observed for bubbles in a highly degassed SA85. (c) (Black line) Temporal evolution of the radius of the bubble ($R_0 = 2.5$ μm; $p_a^0 = 1.45$ bar). (Solid green line) Module of the history force acting on the bubble in the radial time scale. (Dotted green line) Module of the primary Bjerknes force. (d) (Black line) Temporal evolution of the radius of the bubble ($R_0 = 7.6$ μm; $p_a^0 = 2.52$ bar). (Solid green line) Module of the history force acting on the bubble in the radial time scale. (Dotted green line) Module of the primary Bjerknes force. (e) Module of the primary Bjerknes force in a time scale of spatial trajectories. The simulations were made during 10 000 radial cycles. (Blue line) Case ($R_0 = 2.5$ μm; $p_a^0 = 1.45$ bar). (Red line) Case ($R_0 = 7.6$ μm; $p_a^0 = 2.52$ bar). (f) Module of the history force in the time scale of spatial trajectories. The simulations were made during 10 000 radial cycles. (Blue line) Case ($R_0 = 2.5$ μm; $p_a^0 = 1.45$ bar). (Red line) Case ($R_0 = 7.6$ μm; $p_a^0 = 2.52$ bar).

range of p_a^0 [Fig. 9(a) and Fig. 9(b)]. Furthermore, the forces behave as in the high concentration case [Figs. 9(c), 9(d), 9(e), and 9(f)] but with a smaller amplitude.

V. PATH SUPPRESSION BY DRIVING THE BUBBLE WITH A MULTIFREQUENCY EXCITATION

Urteaga and Bonetto [6] show that a moving bubble in a SA85 solution could be spatially fixed by the addition of the 5th harmonic to the fundamental pressure field. The spatial fixing could be obtained for several kinds of harmonics. Figure 10 shows the fitting with the present model of experimental data of the temporal evolution of the radius of an argon bubble in SA85 by minimizing the χ^2 function. The measurements were made by using the Mie scattering technique using a photomultiplier Oriel 77340 with a characteristic response time of FWHM = 2.1 ns. The gray dots in Figure 10 result from the averaging of 10 series. The experiment was carried out with a spatially fixed bubble by the addition of the 7th harmonic. The fundamental driving frequency was similar to the eigenfrequency associated with the first normal mode of the resonator ($f_0 = 29\,081$ Hz). In the sequence of Figs. 11(b)–11(j), the trajectories of the bubble with the same parameters as in the experiment are displayed from a single fundamental

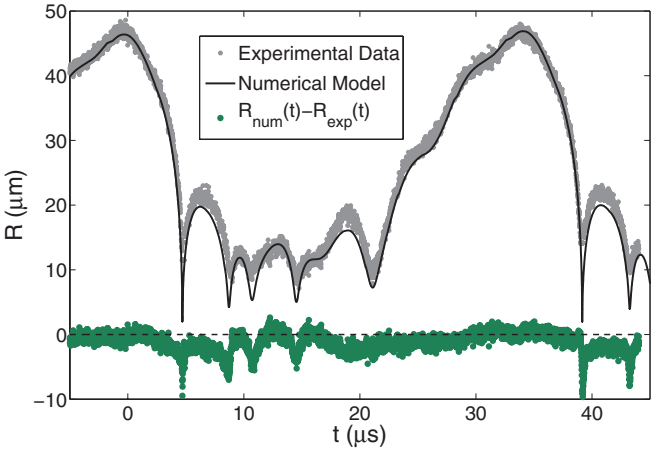

FIG. 10. (Color online) (gray) Bubble radius temporal evolution measured with Mie scattering technique of an argon bubble in SA85 solution driving under bi-harmonic excitation ($f_0 = 29081$ Hz and $f_7 = 7f_0 = 203567$ Hz). (Black) Numerical fitting with the present model. Fitted parameters: $R_0 = (10.7 \pm 0.1)$ μm, $p_a^{bLF} = (1.34 \pm 0.02)$ bar, $p_a^{bHF} = (1.19 \pm 0.02)$ bar, $\phi = (1.80 \pm 0.01)$ rad. The concentration of gas in the liquid is equivalent to $\frac{c_\infty}{c_0} = 0.030$. The time reference $t = 0$ is the zero crossing of the acoustic pressure in the fundamental mode with positive slope.

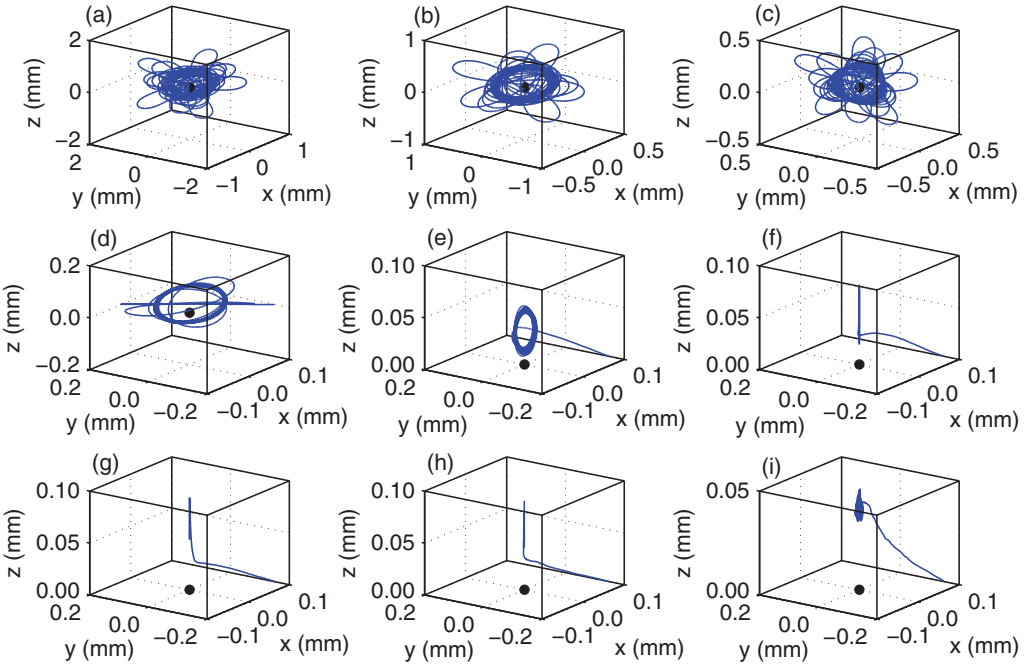

FIG. 11. (Color online) Simulated trajectories for the experimental case shown in Fig. 10. The initial conditions for the system of equations Eqs. (1) are as follows: $R_i = R_0$, $\dot{R}_i = 0.0\frac{\mathrm{m}}{\mathrm{s}}$, $T_b^i = T_{\mathrm{liq}}$, $x_i = 0.10$ mm, $\dot{x}_i = 0.0\frac{\mathrm{m}}{\mathrm{s}}$, $y_i = -0.15$ mm, $\dot{y}_i = 0.0\frac{\mathrm{m}}{\mathrm{s}}$,$z_i = 0.0$ mm, $\dot{z}_i = 0.0\frac{\mathrm{m}}{\mathrm{s}}$. (a) Bubble driving by the fundamental mode only, $p_a^7 = 0.00$ bar. (b) $p_a^7 = 0.15$ bar. (c) $p_a^7 = 0.30$ bar. (d) $p_a^7 = 0.45$ bar. (e) $p_a^7 = 0.50$ bar. (f) $p_a^7 = 0.55$ bar. (g) $p_a^7 = 0.60$ bar. (h) $p_a^7 = 1.05$ bar. (i) $p_a^7 = 1.19$ bar. Spatially fixed bubble by biharmonic excitation within 6 μm. This size of trajectories is of the order of the bubble ambient radius and this movement is considered negligible from the experimental point of view.

driving frequency up to an addition of 7th harmonic with the amplitude given by the previous fitting. It can be seen how the trajectories are gradually suppressed when p_a^7 rises and the mean levitation distance approaches towards the center. The last effect could be explained because the addition of a second harmonic frequency causes larger gradients of the pressure field [Figs. 12(a) and 12(b)]. This means that the averaged primary Bjerknes force in a radial period is greater for a biharmonic driving bubble (spatially fixed bubble) than for a single driven bubble (moving bubble) [Fig. 13(a)]. The

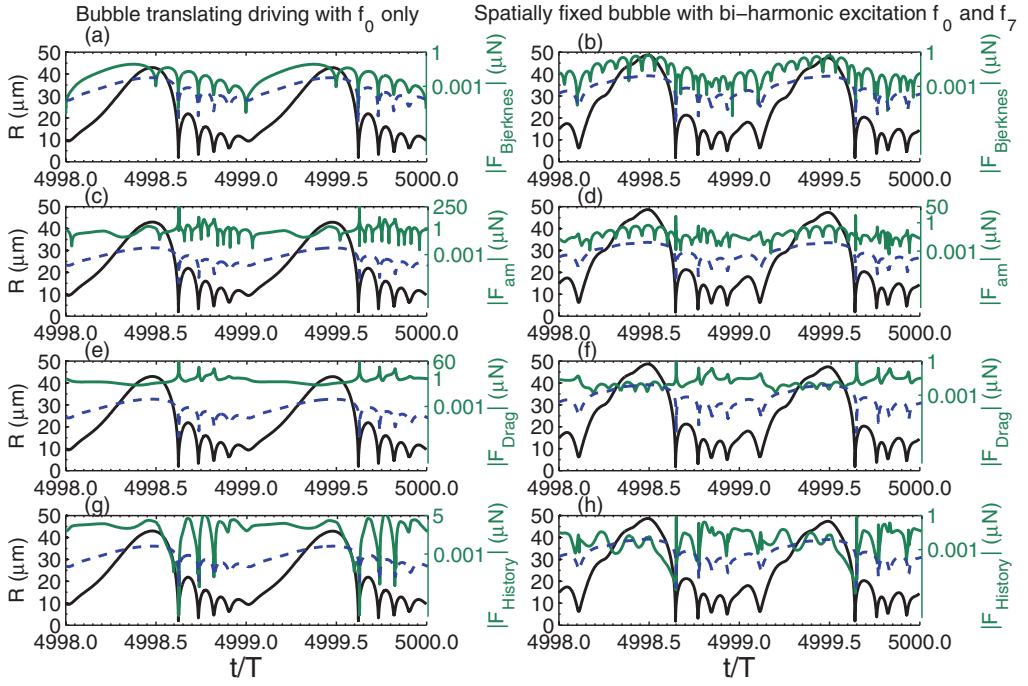

FIG. 12. (Color online) (Green) Module of the forces acting on an argon bubble in SA85 in the time scale imposed by ultrasound. (Blue) Buoyant force. (Black) Temporal evolution of the radius of the bubble.

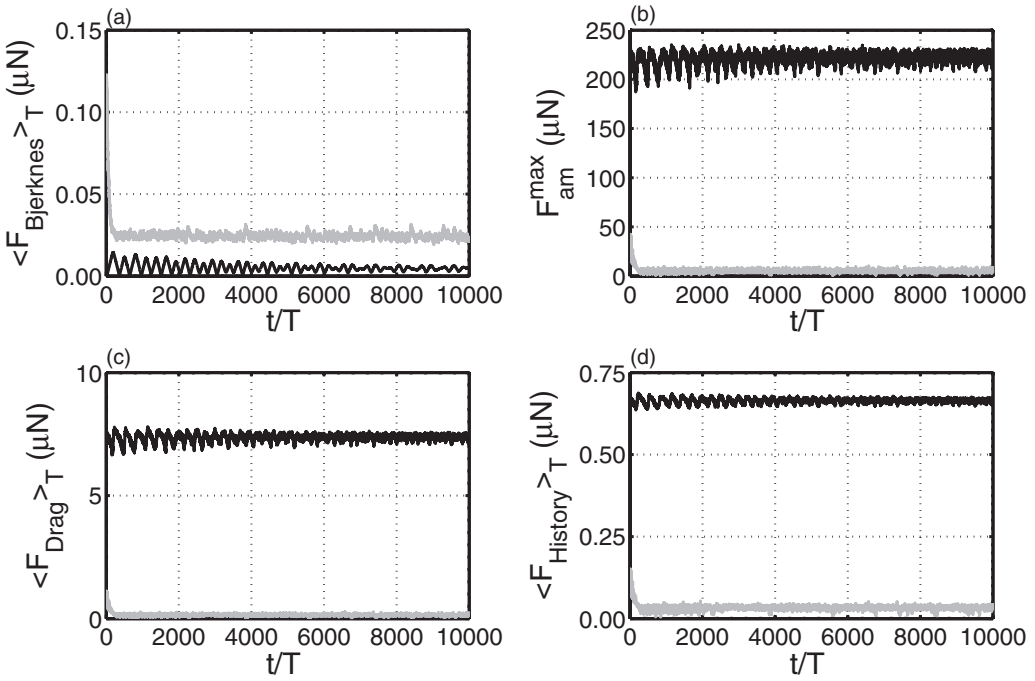

FIG. 13. Forces acting on an argon bubble in SA85 during 10 000 radial cycles (∼0.344 s). (Black line) Bubble driving by only the fundamental frequency f_0. Moving bubble according to case (a) of Figure 11. (Gray line) Bubble under biharmonic excitation with f_0 and $7f_0$. Nonmoving bubble according to the case (i) of Fig. 11.

reduction of the trajectories is the result of the addition of a harmonic that causes a drastic decrease of the maximum added mass peak during main collapse [Figs. 12(c) and 12(d)]. Because of this, the spatial displacements of a bubble under a biharmonic excitation are smaller than the displacements for a single-frequency driving bubble [Fig. 13(b)]. Further analysis of the numerical results show that the biharmonic excitation causes the history force averaged in a radial period to decrease in a 95% respect to the single-frequency driving case [Fig. 13(d)]. It is important to mention that in all cases the shape instability was simulated along the bubble path to check if the pinching of the bubble occurs. In the presented cases the bubbles are parametrically and Rayleigh-Taylor stable following the scheme in Ref. [30] but for periodic driving bubbles.

VI. CONCLUSIONS

In this paper different methods to suppress the trajectories described by a strongly collapsing bubble in a viscous sulfuric acid solution have been numerically and experimentally investigated. To get spatially stationary bubbles is a key fact to have accurate calculations of the temperature acquired by the gas contents inside the bubble, as well as to maximize the energy concentration by trapping small bubbles generated in strongly degassed viscous liquid where no path instability could be detected. For low gas concentration, higher driving pressures on bubble wall could be applied. We note that in order to achieve a good agreement between theory and experiment, it is essential to keep constant the concentration of gas in the liquid in the simulations because that parameter is the one that is controlled and is constant in a real experiment when the amplitude of the pressure field rises. We also point out that in order to simulate the path instability, is necessary to solve the dynamics with the smallest time scale required to reproduce the main collapse of the radial dynamics. The present numerical implementation provides a method to calculate the magnitude of the history force at each time instant, which is not negligible in comparison with the primary Bjerknes force. The consistency of the model has been tested by numerical fittings with experiments of spatially fixed bubbles. For biharmonic excitation it was shown that the trajectories of argon bubbles in SA85 solution could be reduced with a different mode than previous reported experimental results.

ACKNOWLEDGMENTS

L.M.R. acknowledges support from the Argentinian National Council for Scientific and Technological Research (CONICET). We also thank G. Mato and D. Zanette for interesting discussions. We gratefully acknowledge M. del C. Ferreiro for technical support. We appreciate the constructive comments and valuable observations made by the anonymous reviewers.

APPENDIX A: HISTORY FORCE KERNEL APPROXIMATION

To calculate the history force we made the following approximation of the kernel $K(t,\tau)$ of the integral

$$K(t,\tau) = \exp(H)\mathrm{erfc}(\sqrt{H}) \simeq \frac{a}{(a-1)\sqrt{\pi H} + \sqrt{\pi H + a^2}}. \tag{A1}$$

In Eq. (A1), the constant is $a = 2.9110$. This value for a is selected as the one that minimizes the relative error and H denotes the integrals $H = 9\nu_l \int_\tau^t \frac{1}{R^2(s)} ds$. Figure 14 shows

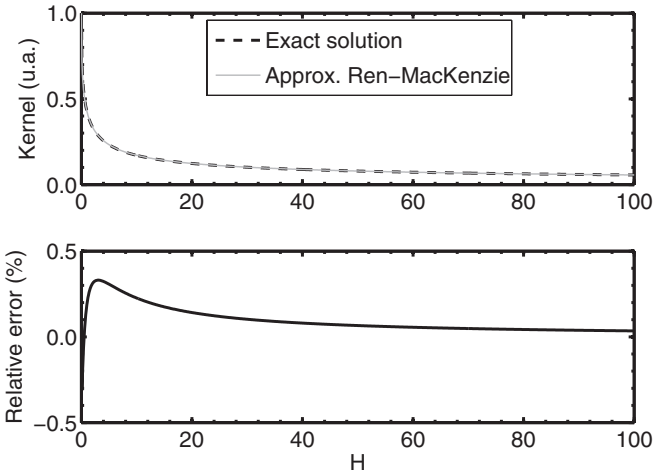

FIG. 14. Solution of the history force kernel model made by Magnaudet and Legendre [13] and the approximation proposed by Ren and MacKenzie [18].

the value of the kernel used in the model of Magnaudet and Legendre [13] and the approximation using the form of Ren and MacKenzie [18]. For a wide range of H values, the relative error is less than 0.3%. In the upper panel of Fig. 14, the type of convergence of the kernel can be seen. In particular, when $H \to \infty$ then $K(t,\tau) \to 0$. This implies that the contributions to the force at the present time from very previous times are

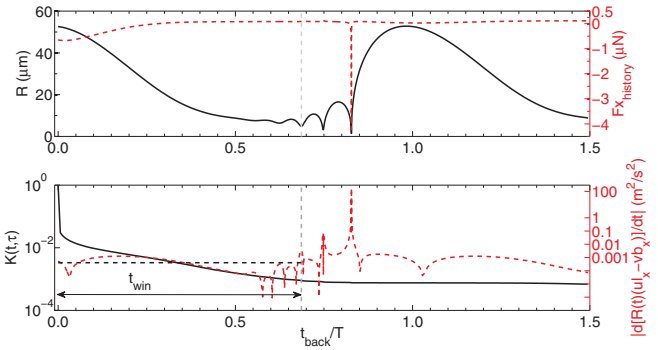

FIG. 15. (Color online) (upper panel) The solid black line is the radius of the bubble at previous times calculated with the numerical model considering the coupling between the radial and translational dynamics but without the feedback of the history force. The red dotted line is the history force in the x direction on the bubble at maximum expansion ($t_{\text{back}} = 0$) calculated with different numbers of points backwards. The parameters of the argon bubble in SA85 are: $R_0 = 9.0$ μm and $p_a^0 \simeq p_a^b = 1.65$ bar at $f_0 =$ 30.0 kHz. (Lower panel) The solid black line indicates the value of the kernel approximated by Ren-Mackenzie form in logarithmic scale. With red dotted line is shown the absolute value of $\frac{d[R(t)\bar{U}_x(r,t)]}{dt}$ in logarithmic scale. For the time interval defined by 400 points backwards (equivalent to t_{win}), indicated with gray dotted line, the variations of $\frac{d[R(t)\bar{U}_x(r,t)]}{dt}$ are rather small compared with the variation during main collapse. The variations are lower than 0.03% from the mean value indicated with black dotted line. During this time interval the "window model" used to calculate the history force is valid according to Ref. [20]. This analysis is similar for the y direction and z direction.

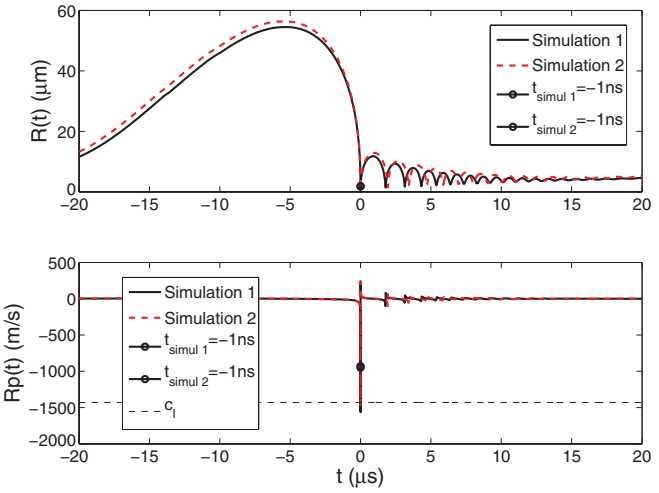

FIG. 16. (Color online) (Upper panel) Temporal evolution of the radius of an argon bubble in water at a temperature of 6 °C. The noncondensible gas, the liquid and driving parameters are the same that the ones reported in Ref. [31] ($f_0 = 19570$ Hz, $p_a^b = 1.28$ bar, $p_\infty = 0.95$ bar, $c_w = 1430$ m/s, $\mu_w = 0.0015$ Pa s, $\sigma_w = 0.075$ N/m, $\rho_w = 999.94$ kg/m^3). (Solid black line) Simulation (1) with an ambient radius $R_0 = 5.0$ μm. (Red dotted line) Simulation (2) with an ambient radius $R_0 = 5.5$ μm. (Black dots) Indicate the instant $t = -1$ ns. At $t = 0$ ns the minimum radius is reached by the bubble. (Lower panel) Radial velocity of the bubble interface. (Thin dotted black line) Speed of sound in the liquid.

less important than the contributions from the immediate past time.

APPENDIX B: WINDOW LENGTH DETERMINATION

An important parameter to set when the window method is applied is the length of the window to make the integrations (t_{win}). This time interval must reconcile the computing time of the history force, the validity of the model to reproduce the physical effect and the validity of the method used to solve the history force integral.

Dorgan and Loth [20] indicated in their work that the "window model" is valid if the term $\frac{d(R\bar{U})}{dt}$ that appears in the history integral is nearly constant. Following this criterion, we determined the size of the backward window. According to the model of the history force used in the present work, in which this force is acting during slow radial and translational dynamics, we start the analysis in a fix time when the bubble has a maximum radius and is when the history force will act.

In Fig. 15 we show the previous dynamics of an argon bubble in SA85 with $R_0 = 9.0$ μm and forced by $p_a^0 = 1.65$ bar at $f_0 = 30$ kHz. Figure 15 also shows how the value of the x component of the history force (without the switches), at the time when the bubble has the maximum radius, changes with the amount of time backwards considered to make the calculation. It can be seen that the contribution of this force at any given time is finite. In addition, the very first previous points have the biggest weight and then the biggest contributions to the history force. The variation of $\frac{d(R\bar{U}_x)}{dt}$ is also displayed in the lower panel of Fig. 15. It can be seen that during a 400-point window the variations are small compared

with the variations at main collapse and first and second rebound. With this size of window we are allowed to research the $R_0 = [3.0; 12.0]$ μm and $p_a^0 = [1.2; 2.7]$ bar parameter phase space for argon bubbles in SA85, because the criteria of small variations within the window is conserved.

APPENDIX C: ERROR ANALYSIS ON THE REPRODUCTION OF MAIN COLLAPSE

In this Appendix we calculate the errors on the drag force and added mass force associated with the possible inaccuracy of the numerical results of the present model to reproduce the main collapse. In particular, we focus on the value of $\dot{R}(t)$ during main collapse, that is, the instant at which the drag force and the added mass force behave like a spike, as well as the moment at which larger translational movements are made by the bubble.

To validate in a quantitative way the numerical results of the present model, we compared the results with experimental measurements and simulations reported by Gompf and Pecha [31]. We have made two simulations with the present model:

Simulation (1): We made a simulation with the properties of the noncondensible gas inside the bubble, surrounding liquid and driving parameters indicated in Ref. [31]. In this simulation, 1 ns previous of reaching the minimum radius, the radial velocity is $\dot{R}_{\text{simul }1}(t = -1 \text{ ns}) = -928.3$ m/s, which differs from the reported value in Ref. [31], $[\dot{R}(t = -1 \text{ ns}) = -950 \text{ m/s}]$, by 2.3%. The radius of the bubble is $R_{\text{simul }1}(t = -1 \text{ ns}) = 1.8$ μm, which differs from the reported value in Ref. [31], $[R(t = -1 \text{ ns}) = 1.7$ μm], by 6%. See Figs. 17(a) and 17(b).

Simulation (2): We made a simulation with the properties of the noncondensible gas inside the bubble, surrounding the liquid and driving parameters indicated in Ref. [31], but we only modify the ambient radius 10% [in simulation (1) $R_0 = 5.0$ μm, while in simulation (2) $R_0 = 5.5$ μm] in order that at $t = -1$ ns the value of $\dot{R}$ would be as close as the reported value in Ref. [31], which is $\dot{R}(t = -1 \text{ ns}) = 950$ m/s. We choose to vary the ambient radius because it has a direct effect on the calculation of $\dot{R}$. In this simulation, 1 ns previous of reaching the minimum radius, the radial velocity is $\dot{R}_{\text{simul }2}(t = -1 \text{ ns}) = -949.1$ m/s. See Fig. 17(b).

In Fig. 16 we display both simulations in the time scale imposed by ultrasound, while in Fig. 17 we focus on main collapse time scale. With these simulations, we can calculate the relative error on the added mass force and on the drag force in the following manner:

$$\text{Error}_{F_{\text{am}}} = \left| \frac{\int_{t=-1\text{ns}}^{t=0\text{ns}} \left|F_{\text{am}}^{\text{simul }2}(t)\right| dt - \int_{t=-1\text{ns}}^{t=0\text{ns}} \left|F_{\text{am}}^{\text{simul }1}(t)\right| dt}{\int_{t=-1\text{ns}}^{t=0\text{ns}} \left|F_{\text{am}}^{\text{simul }2}(t)\right| dt} \right| = 0.05 = 5\%$$

$$\text{Error}_{F_{\text{Drag}}} = \left| \frac{\int_{t=-2\text{ns}}^{t=2\text{ns}} \left|F_{\text{Drag}}^{\text{simul }2}(t)\right| dt - \int_{t=-2\text{ns}}^{t=2\text{ns}} \left|F_{\text{Drag}}^{\text{simul }1}(t)\right| dt}{\int_{t=-2\text{ns}}^{t=2\text{ns}} \left|F_{\text{Drag}}^{\text{simul }2}(t)\right| dt} \right| = 0.04 = 4\%$$

The time intervals chosen to make the area calculations include the whole deltiform evolution of the forces. However, to account for an upper limit of the errors, we calculate them

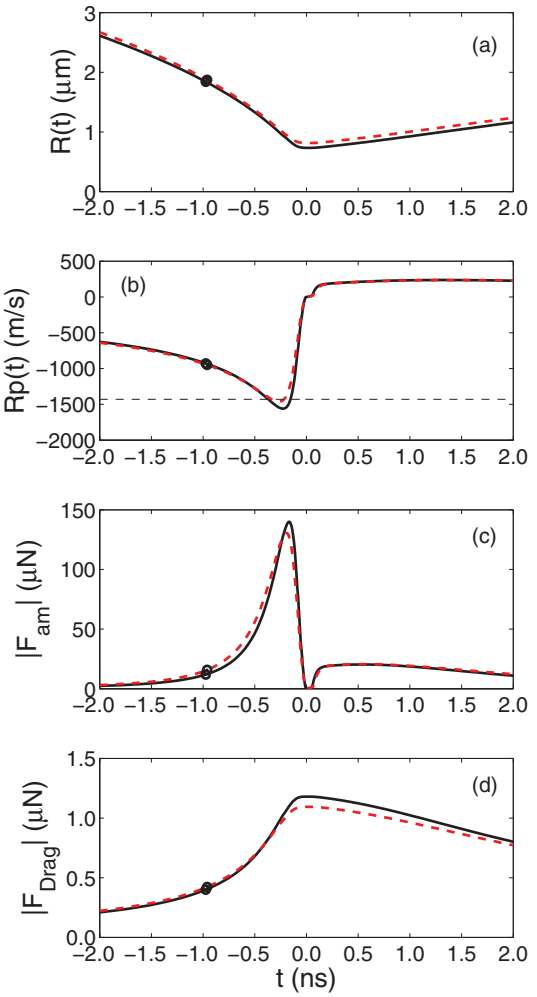

FIG. 17. (Color online) (a) Temporal evolution of the radius of an argon bubble in water, with the liquid and driving parameters reported in Ref. [31]. (Solid black line) Simulation (1) with an ambient radius $R_0 = 5.0$ μm. (Dotted red line) Simulation with an ambient radius $R_0 = 5.5$ μm. (Black dots) Indicate the instant $t = -1$ ns. (b) Radial velocity of the bubble interface. (c) Modulus of the added mass force on the bubble around main collapse. For simulation (1) the maximum value is $F_{\text{am}}^{\text{max}} = 140$ μN while simulation (2) $F_{\text{am}}^{\text{max}} = 130$ μN. (d) Modulus of the drag force on the bubble around main collapse. For simulation (1) the maximum value is $F_{\text{Drag}}^{\text{max}} = 1.18$ μN while simulation (2) $F_{\text{Drag}}^{\text{max}} = 1.09$ μN.

by using the maximum values in Fig. 17(c) and 17(d) in the following manner:

$$\text{Error}_{F_{\text{am}}} = \left| \frac{F_{\text{am}}^{\text{max simul }2}(t = -0.2 \text{ ns}) - F_{\text{am}}^{\text{max simul }1}(t = -0.2 \text{ ns})}{F_{\text{am}}^{\text{max simul }2}(t = -0.2 \text{ ns})} \right| = 0.08 = 8\%$$

$$\text{Error}_{F_{\text{Drag}}} = \left| \frac{F_{\text{Drag}}^{\text{max simul }2}(t = 0 \text{ ns}) - F_{\text{Drag}}^{\text{max simul }1}(t = 0 \text{ ns})}{F_{\text{Drag}}^{\text{max simul }2}(t = 0 \text{ ns})} \right| = 0.08 = 8\%$$

these values are more conservative and are the ones that must be considered. In conclusion, the comparative analysis between the experimentally validated values of $\dot{R}$ from Ref. [31] and the results obtained with the present numerical

model indicates that (i) the proposed model in this work reproduces the values of $\dot{R}$ from Ref. [31] with a 2.3% of error and (ii) this difference of 2.3% in the calculated value of $\dot{R}$ has an impact of less than 8% of relative error in the added mass peak force near main collapse and less than 8% of relative error in the drag force near main collapse.

[1] T. G. Leighton, *The Acoustic Bubble* (Academic Press, San Diego, CA, 1994).

[2] Y. T. Didenko, W. B. McNamara, and K. S. Suslick, Nature **407**, 877 (2000).

[3] D. J. Flannigan and K. S. Suslick, Nature (London) **434**, 52 (2005).

[4] S. D. Hopkins, S. J. Putterman, B. A. Kappus, K. S. Suslick, and C. G. Camara, Phys. Rev. Lett. **95**, 254301 (2005).

[5] R. Urteaga, D. Dellavale, G. F. Puente, and F. J. Bonetto, Phys. Rev. E. **76**, 056317 (2007).

[6] R. Urteaga and F. J. Bonetto, Phys. Rev. Lett. **100**, 074302 (2008).

[7] D. Dellavale, L. M. Rechiman, J. M. Rosselló, and F. J. Bonetto, Phys. Rev. E **86**, 016320 (2012).

[8] H. Xu and K. S. Suslick, Phys. Rev. Lett. **104**, 244301 (2010).

[9] R. Toegel, S. Luther, and D. Lohse, Phys. Rev. Lett. **96**, 114301 (2006).

[10] G. F. Puente and F. J. Bonetto, Phys. Rev. E **71**, 056309 (2005).

[11] G. F. Puente, P. Garcia-Martinez, and F. J. Bonetto, Phys. Rev. E **75**, 016314 (2007).

[12] J. B. Keller, J. Acoustic Soc. Am. **68**, 628 (1968).

[13] J. Magnaudet and D. Legendre, Phys. Fluids **10**, 550 (1998).

[14] L. D. Landau and E. M. Lifshitz, *Fluid Mechanics* (Pergamon Press, London, 1987).

[15] G. K. Batchelor, *An Introduction to Fluid Dynamics* (Cambridge University Press, Cambridge, 1967).

[16] S. Hilgenfeldt, S. Grossmann, and D. Lohse, Phys. Fluids **11**, 1318 (1999).

[17] W. H. Press, S. A. Teukolsky, and W. T. Vetterling, *Numerical Recipies in C: The Art of Scientific Computing* (Cambridge University Press, Cambridge, 1992).

[18] C. Ren and A. R. MacKenzie, Atm. Sci. Lett. **8**, 70 (2007).

[19] L. M. Rechiman, D. Dellavale, and F. J. Bonetto, *Proceedings of the Mecánica Computacional*, edited by A. Cardona, P. H. Kohan, R. D. Quinteros, and M. A. Storti (Asociación Argentina de Mecánica Computacional, Santa Fe, Argentina, 2012), Vol. XXXI, pp. 255–278.

[20] A. J. Dorgan and E. Loth, Int. J. Multiphase Flow **33**, 833 (2007).

[21] E. Loth and A. J. Dorgan, Environ. Fluid Mech. **9**, 187 (2009).

[22] M. A. T. van Hinsberg, J. H. M. ten Thije Boonkkamp, and H. J. H. Clercx, J. Comp. Phys. **230**, 1465 (2011).

[23] B. E. Poling, G. H. Thomson, D. G. Fried, R. L. Rowley, and W. V. Wilding, *Perry's Chemical Engineers' Handbook. Section 2: Physical and Chemical Data*, **8th ed.** (McGraw–Hill, New York, 2008).

[24] T. F. Young and S. R. Grinstead, Ann. N.Y. Acad. Sci. **51**, 765 (1949).

[25] R. C. West and S. M. Selby, *Handbook of Chemistry and Physics* (CRC Press, Cleaveland, 1967).

[26] I. Akhatov, R. Mettin, C. D. Ohl, U. Parlitz, and W. Lauterborn, Phys. Rev. E **55**, 3747 (1997).

[27] M. P. Brenner, S. Hilgenfeldt, and D. Lohse, Rev. Mod. Phys. **74**, 425 (2002).

[28] R. Sadighi-Bonabi, R. Rezaei-Nasirabad, and Z. Galavani, J. Acoust. Soc. Am. **126**, 2266 (2009).

[29] Y. Hao and A. Prosperetti, Phys. Fluids **11**, 1309 (1999).

[30] L. M. Rechiman, F. J. Bonetto, and J. M. Rosselló, Phys. Rev. E **86**, 027301 (2012).

[31] B. Gompf and R. Pecha, Phys. Rev. E **61**, 5253 (2000).

[32] See Supplemental Material at http://link.aps.org/supplemental/10.1103/PhysRevE.87.063004 for a detailed information on supporting experiments at high and low concentration of gas diluted in the liquid.